

Peter H. Wilkins¹

Department of Mechanical Engineering,
Pennsylvania State University,
University Park, PA 16802
e-mail: phw13@psu.edu

Stephen P. Lynch

Department of Mechanical Engineering,
Pennsylvania State University,
University Park, PA 16802
e-mails: splynch@psu.edu;
spl11@psu.edu

Karen A. Thole

Department of Mechanical Engineering,
Pennsylvania State University,
University Park, PA 16802
e-mail: kthole@psu.edu

Tyler Vincent

Pratt & Whitney,
East Hartford, CT 06118
e-mail: tyler.vincent2@prattwhitney.com

San Quach

Pratt & Whitney,
East Hartford, CT 06118
e-mail: san.quach@prattwhitney.com

Dominic Mongillo

Pratt & Whitney,
East Hartford, CT 06118
e-mail: dominic.mongillo@prattwhitney.com

Effect of a Ceramic Matrix Composite Surface on Film Cooling

Ceramic matrix composite (CMC) parts create the opportunity for increased turbine entry temperatures within gas turbines. To achieve the highest temperatures possible, film cooling will play an important role in allowing turbine entry temperatures to exceed acceptable surface temperatures for CMC components, just as it does for the current generation of gas turbine components. Film cooling over a CMC surface introduces new challenges including roughness features downstream of the cooling holes and changes to the hole exit due to uneven surface topography. To better understand these impacts, this study presents flowfield and adiabatic effectiveness computational fluid dynamics (CFD) for a 7–7 shaped film cooling hole with a 5 Harness Satin CMC weave at two orientations. To understand the ability of steady RANS to predict flow and convective heat transfer over a CMC surface, the weave surface is initially simulated without film and compared to previous experimental results. The simulation of the weave orientation of 0 deg, with fewer features projecting into the flow, matches fairly well to the experiment and demonstrates a minimal impact on film cooling leading to only slightly lower adiabatic effectiveness compared to a smooth surface. However, the simulation of the 90-deg orientation with a large number of protruding features does not match the experimentally observed surface heat transfer. The additional protruding surface produces degraded film cooling performance at low blowing ratios but is less sensitive-to-blowing ratio, leading to an improved relative performance at higher blowing ratios, particularly in regions far downstream of the hole.
[DOI: 10.1115/1.4053842]

Keywords: computational fluid dynamics (CFD), heat transfer and film cooling

Introduction

Ceramic matrix composite (CMC) components are becoming more and more prevalent in the aerospace industry. With advantageous thermal and weight properties at high temperatures, CMC's create the opportunity for significant improvements in efficiency compared to traditional metal alloys used in many current-generation gas turbines [1]. This improved performance can be attributed to higher turbine entry temperatures CMCs can withstand which can lead to reductions in the amount of cooling airflow required to meet durability life requirements. An additional advantage stems from the relatively lower densities of CMC components compared to their metal counterparts, enabling lighter turbines and improving thrust-to-weight ratios [2]. To enable the highest turbine entry temperatures possible, the use of film cooling to enable CMC components to withstand operating temperatures beyond their native capabilities will be important.

Film cooling over a CMC surface presents several challenges that are distinct from film cooling over traditional metal components. CMC surface topography differs substantially from the surfaces of metal components with large anisotropic periodic features that have a substantial impact on the flow field [3]. The impact that these features have on film cooling performance will be important to understand in order to take full advantage of CMCs.

This study aims to understand the predictive capability of steady Reynolds-averaged Navier–Stokes (RANS) to evaluate a woven CMC surface with respect to flow field and heat transfer performance. To do this, a conjugate analysis is investigated that replicates the experiment conducted by Wilkins et al. [3]. Then, building off of the conjugate analysis, a computational fluid dynamics (CFD) analysis evaluates the same weave pattern across multiple hole locations and orientations to develop an understanding of some of the impacts the weave has on film cooling.

Background

Over the past few decades, there has been a significant amount of work investigating the performance of film cooling. However, the impact of roughness and other atypical surface geometries has mostly been focused on cylindrical holes over roughness element surfaces [4–8]. The unique characteristics of different types of roughness, as described by Bons [9], highlight the potential to impact film cooling in unexpected ways. Additionally, the low momentum flow leaving a shaped film cooling hole may interact differently than for cylindrical holes without diffusers.

Early experiments investigating the impact of surface roughness on cylindrical non-diffused film cooling were performed by Goldstein et al. [4]. Investigating both single and multi-row cooling, Goldstein et al. saw a dissimilar performance at low and high blowing ratios. Low blowing ratios experience degradation in performance when a rough surface is present, while higher blowing ratios experience an improvement in performance for both single and multi-row configurations.

Building on the work done by Goldstein et al. [4], Barlow and Kim [5] investigated the impact of a simulated rough surface on

¹Corresponding author.

Contributed by the International Gas Turbine Institute (IGTI) of ASME for publication in the JOURNAL OF TURBOMACHINERY. Manuscript received September 1, 2021; final manuscript received January 6, 2022; published online March 4, 2022. Tech. Editor: David G. Bogard.

film cooling at a higher turbulence level of 8.5%. Using cylindrical holes without diffusers, their single row experiments found that the addition of roughness leads to increased mixing due to increased turbulence generated from the rough surface. This increased turbulence leads to a relative degradation in performance compared to a flat smooth surface near the hole and follows a similar trend with increasing blowing ratio leading to a reduction in adiabatic effectiveness. While this trend does continue in an area-averaged sense, locally further downstream the increased turbulence leads to up a 50% improvement over a flat plate at higher blowing ratios. The other aspect of Barlow and Kim's [5] publication focuses on the impact that roughness has on convective heat transfer coefficients when film cooling is present. Here, they find that while film cooling does increase the heat transfer coefficient for both smooth and rough surfaces, the rough surfaces have a smaller relative increase due to their already elevated turbulence levels.

Focusing on the impact that turbine-specific roughness has on film cooling, Schmidt et al. [6] investigated different scales of turbine appropriate roughness for cylindrical holes without diffusers. With their lower roughness case showing degradation in centerline effectiveness across the range of blowing ratios, but at their higher blowing ratio, the rougher case saw improved performance along the centerline compared to a flat surface, showing improvement can be seen even along the centerline not just in a laterally averaged sense as specified previously. Taking this experiment a step further, Schmidt and Bogard [7] introduced a high level of free-stream turbulence to the lower roughness case previously tested by Schmidt et al. [6]. At this higher turbulence level of 17%, the rough surface outperforms the smooth case across all of the blowing ratios tested, showing that the increased turbulence produced by a rough surface helps pull coolant back to the wall improving cooling performance.

Lawson and Thole [8] investigated the impact of simulated film cooling with particle deposition at high turbulence level of 12.3%. The deposition was simulated across cylindrical holes without diffusers at multiple blowing ratios showing degradation in film cooling across all the conditions tested. However, the higher blowing ratio saw a degradation in film cooling smaller than the lower blowing ratios, which the authors attribute to the already low performance at the higher blowing ratio resulting in little change.

A variety of computational studies have been performed investigating the impact that rough surfaces have on surface flow and heat transfer. Wang et al. [10] investigated the ability of RANS to predict skin friction coefficient and St over various rough surfaces. Using a Spalart-Allmaras turbulence model, Wang et al. found that RANS was able to predict the skin friction coefficient within 3.5% and the Stanton number within 8–15%, with the predictions for cases with larger surface features residing at the higher end of that range [10]. Bons et al. found larger disagreements between experimental and computational results, with skin friction and Stanton number deviating by 8% and 17%, respectively [11].

Hanson et al. [12] investigated the impact that different types of roughness elements have on the predictive capability of RANS. They looked at scaled-up true roughness and two different types of simulated roughness using elliptical cones and ellipsoids. Hanson et al. [12] found simulations with true roughness matched experimental data, the elliptical cone cases were within 15%, while the CFD ellipsoid cases differed from their experimental counterparts by approximately 50%. The authors believed this large difference was due to the transverse interaction between the roughness elements and the surface creating a challenge for the RANS models.

Investigations into the impact directional roughness elements have on aerothermal characteristics of a surface was performed by Kapsis and He [13] using multiple RANS models in addition to large eddy simulations (LES). They found directional elements produced unique flow features that were dependent on the shape and cannot be replicated by stochastic roughness. These unique features

were found across both transitional and turbulent flow regimes and suggest that single roughness parameters like Ra can be inadequate.

Computational film cooling work has been mainly focused on the explaining underlying physics of film cooling in regions that are difficult and/or impossible to measure experimentally [14–16]. This is because in order to close the turbulence equations in a RANS solution, several assumptions must be made, including the assumption that eddy viscosity is isotropic. This assumption is not appropriate for film cooling flows of course. But despite this, some regions are well captured by RANS including the in-hole region and the pattern of coolant at the hole exit [16].

Harrison and Bogard [17] investigated the impact that cylindrical holes without diffusers embedded in a narrow trench have on adiabatic cooling effectiveness. They found that RANS predictions when a trench was present often resulted in more accurate CFD predictions than cylindrical holes alone and were able to accurately capture the resulting increased spreading in adiabatic effectiveness by the trenches compared to cylindrical holes. Haydt and Lynch [18] investigated a 7–7–7 diffused shaped hole geometry at a variety of compound angles. They found that holes at high blowing ratios see improved attachment and increased lateral spreading at large compound angles. CFD simulations of the experimental test cases indicated regions of high vorticity accompany these locations of increased lateral spreading at high blowing ratios.

In this study, using CFD analysis, we simulate the convective heat transfer and film cooling on a unique surface roughness created by the regular wavy pattern of a ceramic matrix composite material. To our knowledge, no information currently in literature compares the ability of design tools such as RANS to predict these quantities. Furthermore, there is currently no understanding of how this surface impacts film cooling behavior.

Description of Surface Geometry

To simulate a CMC surface, a mathematically defined 5 Harness Satin (5HS) weave pattern originally described by Nemeth et al. [19] was chosen. This weave pattern is modified as described by Wilkins et al. [3] to create a repeating unit cell (RUC) that is anisotropic and periodic in nature shown in Fig. 1. The RUC has a base tow width of 1.125 mm and a base fabric thickness of 0.375 mm. This geometry is then scaled and used for both the conjugate and film cooling analyses shown in Fig. 2, which comprises of long “A” tows and shorter “B” tows that cross over the “A” tow once every fifth weave.

In the case of the conjugate heat transfer analysis, the surface is scaled up 30× to achieve engine-relevant Re and aligned to match the test cases examined by Wilkins et al. [3]. The resulting computational geometry is longer and wider than the surface examined by Wilkins et al. to allow boundary layer development to match Re and allow for the entire width of a unit cell to be present enabling

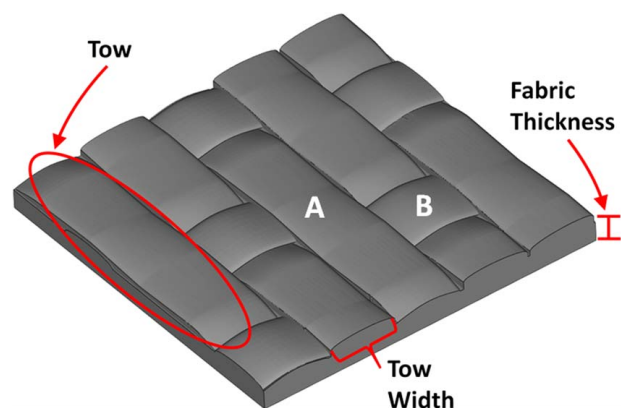


Fig. 1 5 Harness Satin repetitive unit cell or the CMC weave pattern

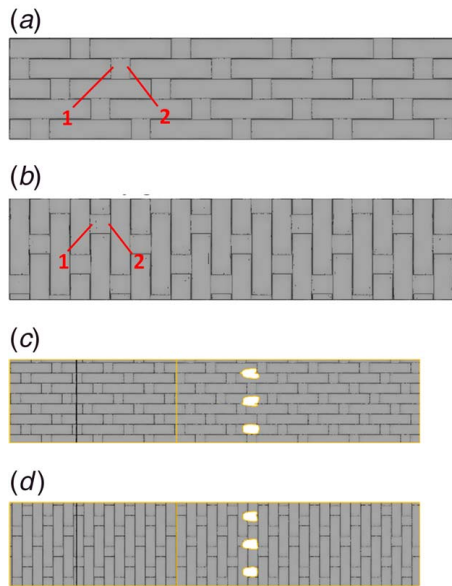


Fig. 2 Surface profiles of CMC surfaces in (a) 0-deg conjugate, (b) 90-deg conjugate, (c) 0-deg film cooling, and (d) 90-deg film cooling models

periodic boundary conditions along the edges. Below the CMC surface is a thin silicone interface that was used by Wilkins et al. to ensure full thermal contact between the CMC plate and the constant temperature source and is present in the model to ensure consistency between the computational and the experimental results. Two cases are examined, one with the long-exposed tows parallel to the freestream, called the 0-deg orientation, and the other with the long-exposed tows perpendicular to the freestream, called the 90-deg orientation, shown in Figs. 2(a) and 2(b), respectively.

The film cooling geometry is based around the use of the 7–7–7-shaped hole introduced by Schroeder and Thole [20] and shown in Fig. 3. The meter diameter of the 7–7–7 hole for this study is 7.75 mm, the same meter diameter that was used in Schroeder and Thole [20]. Exit planes for the holes were aligned to the mean roughness height of the CMC surface resulting in distinct outlet profiles that can be observed in Figs. 2(c) and 2(d). To scale the CMC surface, the film cooling holes use a nominal engine scale hole meter diameter of 0.52 mm, resulting in an increase in an scale of 15× for the system. The resulting roughness values for the 15× scale CMC surface are $S_a = 0.57$ mm, $S_q = 0.70$ mm, and $S_z = 3.01$ mm relative to the mean roughness height.

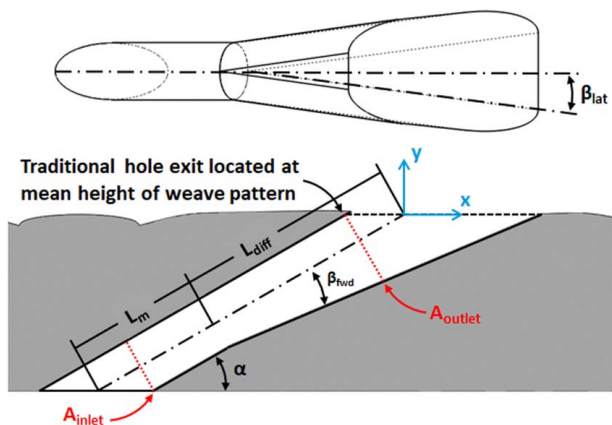


Fig. 3 7–7–7 film cooling geometry, developed by Schroeder and Thole [20]

Each film cooling domain is composed of three film cooling holes with a $P/D = 6$ resulting in a total width of 18D. The scaled RUC was then used to create two film cooling surfaces similarly to the conjugate geometries. One has the long-exposed “A” tows oriented parallel to the freestream, called the 0-deg orientation shown in Fig. 2(c). The other surface has the long-exposed “A” tows oriented perpendicular to the freestream, which is the 90-deg orientation shown in Fig. 2(d). For both geometry cases, a contoured boundary layer trip 1.27-mm tall located at $x/D = -35$ ensures a turbulent boundary condition. The entrance region extends to $x/D = -50$ in front of the holes and the film cooling region extends to $x/D = 35$ downstream of the holes.

A third film cooling geometry provides a smooth surface as a baseline case from which to compare the CMC cases. This geometry has one hole and is 6 diameters wide rather than the three-hole models of the CMC cases, and the upstream region only extends to $x/D = -34$. Besides the previously mentioned deviations, the flat geometry is identical to the CMC film cooling cases.

Computational Methods

Two different types of cases are examined computationally in this study. First is a conjugate analysis that aims to recreate the exact conditions shown by Wilkins et al. [3] to calculate Stanton number. In pursuit of this goal, the domain of the conjugate analysis can be broken up into three distinct regions shown in Fig. 4. The bottom layer is a silicone interface material that has a constant temperature boundary condition applied at its base with adiabatic wall conditions around the edges and interfaces with the CMC surface above it. The CMC surface is a three-dimensional (3D)-printed polycarbonate material with a measured thermal conductivity of 0.208 W/(mK). The bottom of the CMC surface interfaces with the silicone, the sides are adiabatic, and the top of the CMC surface creates an interface with the fluid region passing over the surface. Meshes for the silicone and CMC surface are derived from the unstructured meshes used by Wilkins et al. [3].

Directly on top of the CMC surface is the fluid region which is composed of room temperature air. This region has a constant velocity inlet boundary condition with the freestream velocity taken from Wilkins et al. [3]. To prevent the constant velocity inlet condition from generating artificial accelerations over the CMC surface at the inlet plane, velocity inlet locations with a y height less than the maximum y height of the CMC surface are given a zero velocity. Between the zero and freestream velocities, a small transition region is present. Both sides are given periodic boundary conditions to account for the repeating nature of the CMC RUC, and the top of the fluid region is a wall with a slip boundary condition. The mesh for this region is generated using an unstructured mesh with

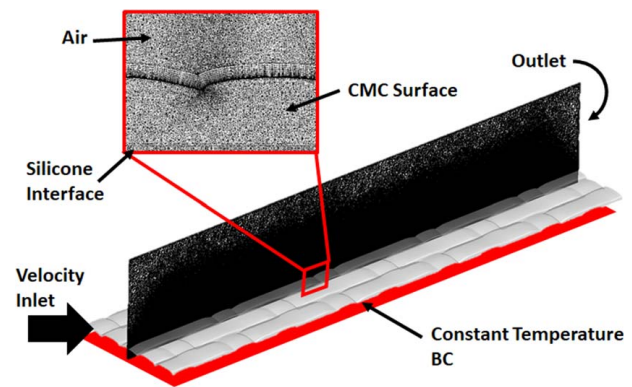


Fig. 4 Isometric view of 0-deg 5HS conjugate test case with centerline mesh, CMC surface, and selected boundary conditions

boundary controls focusing most of the resolution down near the fluid–solid interface.

The local St on the surface of the CMC is calculated in the same way as described by Wilkins et al. [3]. First, the local heat transfer coefficient across the surface is calculated

$$h(x, z) = \frac{q''(x, z)}{T_s(x, z) - T_\infty} \quad (1)$$

One notable difference between Eq. (1) and Wilkins et al. [3] is that Eq. (1) uses the total boundary heat flux because no radiation is modeled in the domain. The heat transfer coefficient is then nondimensionalized using the freestream density, specific heat capacity, and velocity to obtain the Stanton number.

To ensure grid independence, the 0-deg heat transfer case was analyzed with 11×10^6 , 18×10^6 , and 20.5×10^6 cell meshes. Comparisons of the local and average St indicated a maximum difference of 0.5% between the three levels, suggesting that the solution was independent of grid size.

The film cooling analysis is broken up into two parts: the first is the flow development region which allows the boundary layer to grow to an appropriate thickness, and the second is the film cooling region that takes the developed boundary layer and introduces three film cooling holes in the CMC surface. This approach allows for multiple cooling conditions to be evaluated for a given geometry without the need to rerun the entire domain each time. The boundary layer development region is between $x/D = -50$ and $x/D = -15$ and develops a boundary layer over a similar length to the results presented by Eberly and Thole [21]. The inlet for the flow development region has a temperature of 328 K and a mainstream velocity of 10 m/s. Like the conjugate analysis, inlet locations with a y height less than the maximum y height of the CMC surface are given zero velocities with a small transition between the zero and freestream velocities. Because the domain width of 18 diameters does not align with the periodicity of the CMC RUC at the model scale, symmetry boundary conditions are used along the edges rather than periodic boundaries; this is not expected to impact the solution around the film cooling holes which are not close to the domain sidewalls. An adiabatic wall with a slip condition is used for the top of the domain, and an adiabatic wall is used for the CMC surface. The mesh for the flow development region uses an unstructured mesh with surface controls causing most of the cells to be focused near the CMC wall.

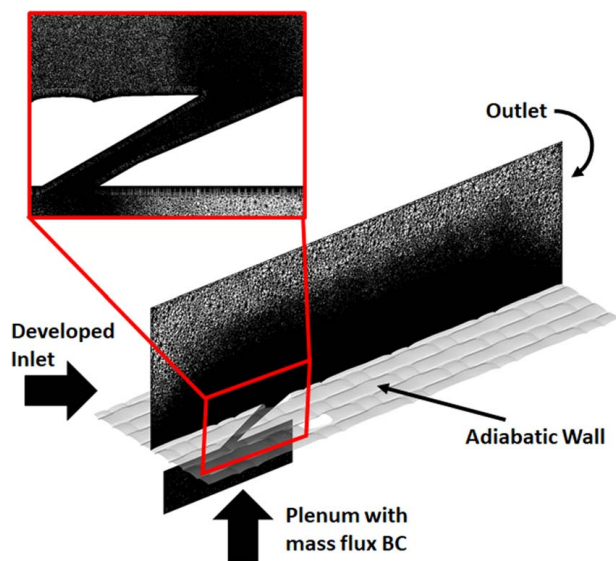


Fig. 5 Isometric view of 0-deg 5HS film cooling test case with centerline mesh, CMC surface, and selected boundary conditions

A grid independence study was performed on the entry region of the 0-deg surface with 2.8×10^6 , 4.2×10^6 , and 6.6×10^6 cells, and the maximum difference in the skin friction coefficient was less than 0.5%.

Starting at $x/D = -15$ and extending downstream to $x/D = 35$, the film cooling region consists of three main parts, the freestream domain, the holes, and the coolant supply plenum as shown in Fig. 5. For the freestream boundary conditions, the inlet uses the turbulence and velocity information from the flow development region model described earlier, the sides use symmetry boundary conditions, the CMC surface is an adiabatic wall, and the top is an adiabatic wall with a slip condition. The film-cooled CMC surface is modeled as an adiabatic wall. In the plenum, an adiabatic boundary condition is used along the top, forward, and rear-facing walls. The sides of the plenum use symmetric boundary conditions. The bottom of the plenum is a mass flow inlet with cold air at 218 K to achieve a density ratio (DR) of 1.5 and a mass flowrate dependent on the desired blowing ratio. The same unstructured meshing strategy is employed for the flow development region, with boundary controls to focus the cells near the wall and in the hole. A grid independence study was performed using 8.6×10^6 , 11.6×10^6 , and 20.5×10^6 cell grids, with a maximum deviation in average η of 0.004 between all cases.

A flat plate baseline case is evaluated for a single film cooling hole, with one notable difference in the inlet boundary layer. A previously measured boundary layer profile from the wind tunnel described in Eberly and Thole [21] is used as the inlet boundary condition, instead of the computationally developed boundary layer over the CMC surface upstream of the hole.

Both the conjugate heat transfer and the adiabatic film cooling models are evaluated using a steady RANS segregated solver, with second-order accuracy in gradient discretization and a realizable two-layer $k-\epsilon$ turbulence model. This model was selected based on improved accuracy in film cooling over other models as seen in literature [22–24]. Near the wall, a two-layer all y^+ wall treatment is used with average y^+ values between 0.5 and 1 for all cases investigated. This analysis was completed using the commercial CFD software STAR-CCM+ 14.04.011. The fluid is air, modeled as an ideal gas with temperature-dependent properties. Convergence is evaluated through multiple monitors including equation residuals and average surface temperature in the target area, and cases are run for at least 500 iterations after all monitors have reached constant values.

Results and Discussion

Two CMC weave geometries are analyzed and compared to previous experimental results from Wilkins et al. [3] to determine how well the computational data capture the heat transfer and boundary layer behavior. In regions of reasonable similarity, the computational data are used to further investigate the physics of the near-surface behavior. Then, the same geometries are investigated with film cooling to determine the impact the weave surface has on resulting flow and temperature fields.

Effect of the Ceramic Matrix Composite Weave Features on Heat Transfer. The predictive accuracy of the convective heat transfer from the CFD varies substantially between the two weave orientations, with the 0-deg orientation matching the experimental results more closely. The local heat transfer shown in Fig. 6 is in terms of a percent increase in St relative to a flat plate, where the flat plate value is at the corresponding Re . Figure 7 presents a detailed view of the 0-deg surface, highlighting the St trends around the tow transitions.

On the 0-deg surface, the leading edge of a “B” tow for both the experimental results in Fig. 7(a) and CFD results in Fig. 7(b) indicate increased heat transfer relative to a flat plate. Here, the magnitudes and shapes of the regions of increased heat transfer are similar between the CFD and experimental results, indicating that the CFD

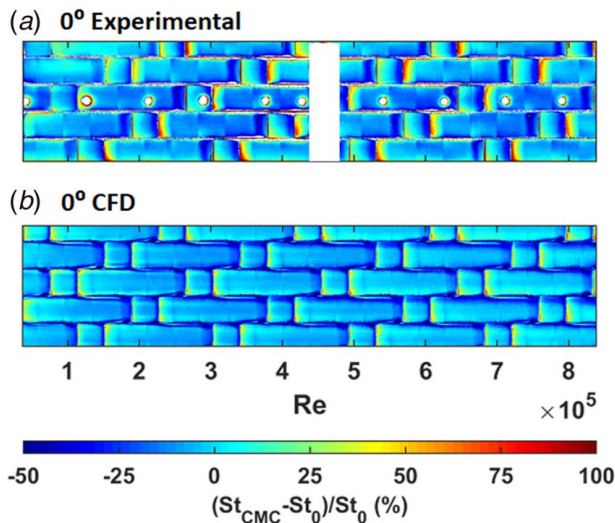


Fig. 6 St augmentation over the 0-deg 5HS surface for the (a) experimental [3] and (b) CFD cases, with velocity boundary layer locations indicated by the numbers

predicts this region well. The other region that indicates a relative increase in heat transfer compared to a flat plate is the upstream side of “A” tows. In Figs. 7(a) and 7(b), the experimental and CFD results have positive augmentation regions similar in shape but differ in magnitude. St augmentation on the front of “A” tows in Fig. 7(b) indicates lower levels of heat transfer compared to the experimental results in Fig. 7(a). This underprediction may be due to unsteadiness not captured in RANS.

Regions of low heat transfer compared to a flat plate are also present over the 0-deg CMC surface. On the downstream side of “A” tows, regions of negative augmentation are present across the surfaces shown in Fig. 6. From the magnified representative sections in Fig. 7, the experimental results indicate lower heat transfer (more negative augmentation) than the CFD. Negative augmentation is also present on the downstream facing surface of “B” tows for both surfaces. Here, the augmentation in the experimental results in Fig. 7(a) is also more negative compared to the CFD in

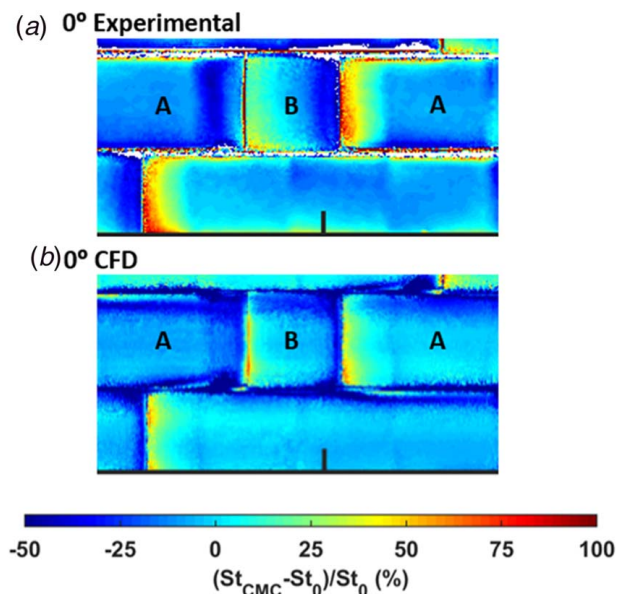


Fig. 7 Magnified view of St augmentation over the 0-deg 5HS surface for the (a) experimental [3] and (b) CFD cases

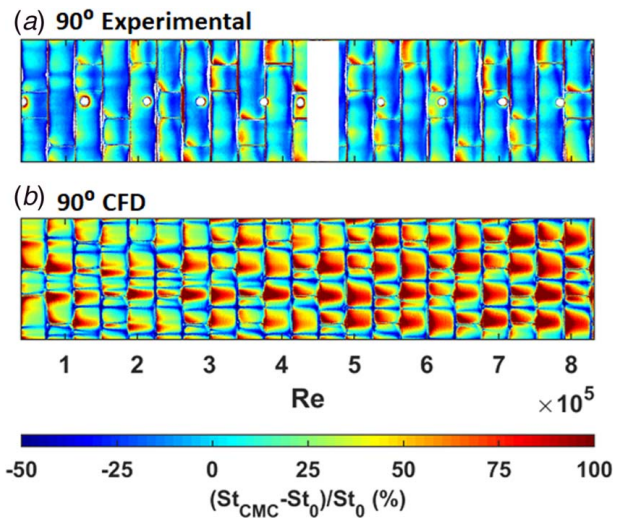


Fig. 8 St augmentation over the 90-deg 5HS surface for the (a) experimental [3] and (b) CFD cases

Fig. 7(b). In these two regions, CFD underpredicts the reduction in heat transfer, potentially due to misprediction of the separated flow that exists in these regions.

While the local trends of the 0 deg surface were generally captured by the CFD, the simulation of the 90 deg surface was not as successful. Shown in Fig. 8, the local St augmentation values for the experimental and CFD results are substantially different in trends and magnitudes. In general, the experimental results shown in Fig. 8(a) highlight regions of high heat transfer relative to a flat plate on the leading edges of tows. These regions are relatively evenly spread across the leading edges of “A” tows, but there is an increase in augmentation when passing over a “B” tow. Regions of low heat transfer compared to a flat plate can be found on the downstream side of tows.

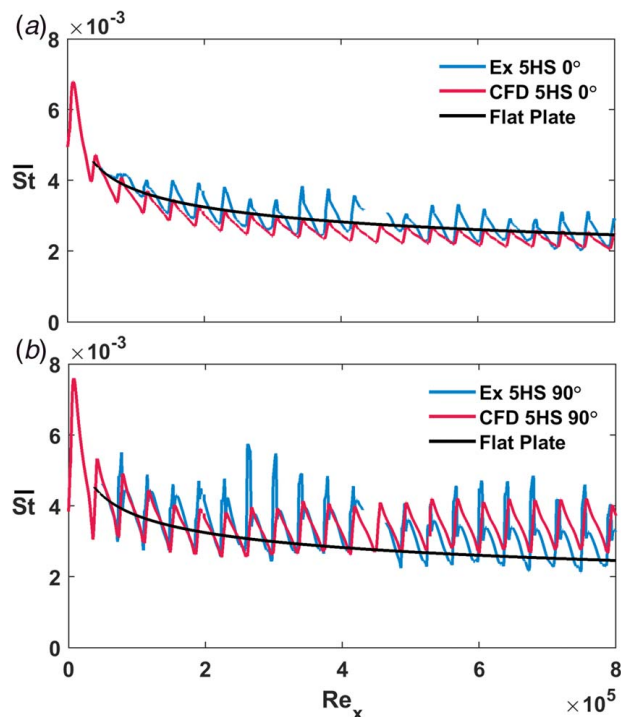


Fig. 9 Laterally averaged St across the (a) 0-deg surface and (b) 90-deg surface

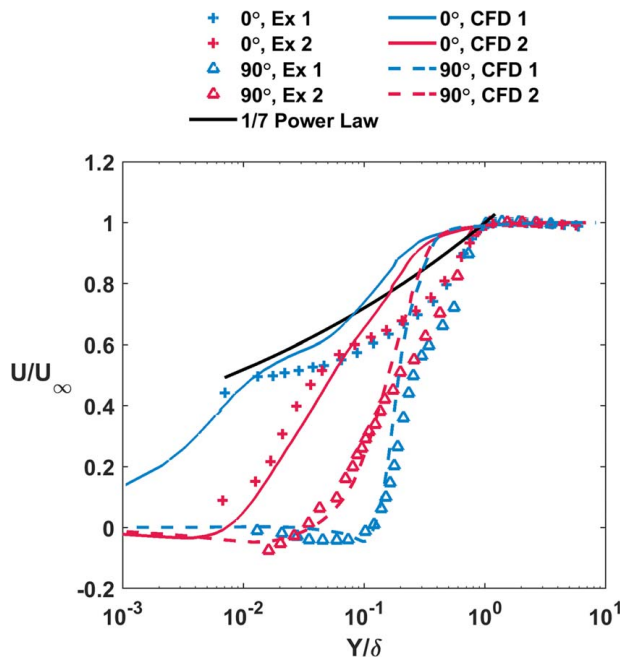


Fig. 10 Nondimensional velocity profiles for both the 0-deg and 90-deg surfaces at locations 1 and 2

The CFD shown in Fig. 8(b) presents some instances of this behavior, particularly in the upstream region where the flow is less developed. However, the dominating features in the CFD are the regions of high heat transfer that are separated by thin streaks of low heat transfer. This distribution is persistent with Re , and as will be shown later, is the result of streamwise vortices generated by the abrupt steps that are re-energized across the tows.

The lateral averages of St along the length of the surface for both orientations result in similar patterns. Figure 9(a) shows that lateral averages for both the 0-deg experimental and CFD results have a similar aligned periodic pattern. Here, the CFD results have lower peaks in St , but share a similar minimum lateral value as the experimental results. Looking at Fig. 9(b) for the 90-deg orientation, the periodicity is well predicted but there is more variation between the magnitude of the CFD and experimental results. At low Re , the CFD predicts similar minimum values as the experimental results, but predicts maximum values lower than the experimental spikes in St at the tow transitions. At $Re > 4 \times 10^5$, the CFD predicts minimum St values that are higher than the minimum values from the experimental results. The deviation in the amplitudes of the periodic behavior is due to the inflated impact of the leading edges of the tows.

Differences observed in the laterally averaged St are also present in the surface area averages. The CFD for the 0-deg orientation

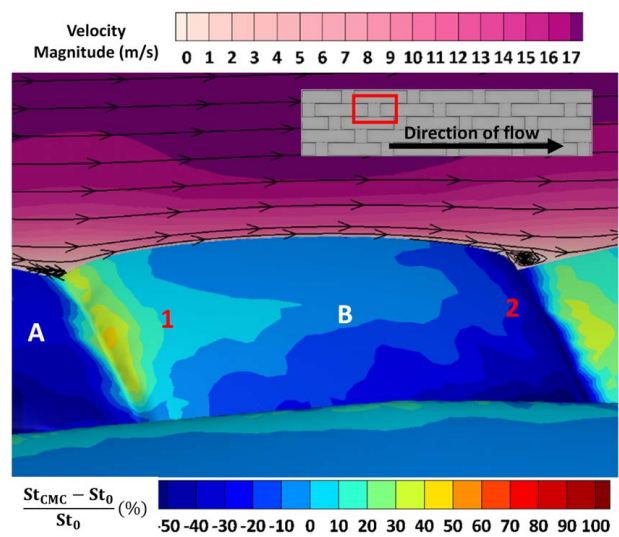


Fig. 11 Contour of St number on the 0-deg CMC surface over which a contour of velocity magnitude is plotted underneath streamlines showing flow direction

predicts a -8% St augmentation value compared to a flat surface, while the 90-deg orientation has a positive 19% augmentation in St . The experimental St augmentation for the 0-deg case is 1% showing the CFD 0-deg prediction of -8% to be an underprediction. This trend is reversed for the 90-deg case with an area St augmentation value of 19% overpredicting heat transfer compared to the 8% measured value. For both cases, the over and underprediction of the area-averaged St within the prediction range is found by Wang et al. [10] and Bons et al. [11].

The prediction of the local velocity boundary layer in the CFD is compared to the experimental boundary layer measurements taken by Wilkins et al. [3]. Boundary layer profile locations 1 and 2 for both the 0-deg and the 90-deg orientations are shown in Figs. 2, 6, and 8. In Fig. 10, the nondimensional boundary layer velocity profiles are plotted against nondimensional wall distance at locations 1 and 2 for both the 0-deg and 90-deg orientations. Boundary layer thickness is determined by the height at which 99% of the free-stream velocity is reached. Here, the velocity profiles are not plotted in inner coordinates because the wall shear stress was not measured in the experimental results of Wilkins et al. [3].

Starting with the 0-deg case in Fig. 10, a good agreement can be seen at locations 1 and 2 in the lower boundary layer until $Y/d = 0.05$, at which point the velocity increases rapidly within the boundary layer likely due to the underdevelopment of the momentum and displacement thicknesses by up to 50% relative to the experimental results, as shown in Table 1. This underdevelopment of the boundary layer is likely due to the lower turbulence generated by the CMC surface in the CFD compared to the experimental results. The

Table 1 Summary of boundary layer measurements

Weave orientation	0-deg Orientation				90-deg Orientation			
	Experimental		CFD		Experimental		CFD	
Location	1	2	1	2	1	2	1	2
Distance from leading edge (x/λ_{30})	5.13	5.81	5.13	5.81	3.94	4.95	3.94	4.95
Distance from centerline (z/λ_{30})	0.89	0.89	0.89	0.89	1.13	1.13	1.13	1.13
Re_x	2.00×10^5	2.26×10^5	2.00×10^5	2.26×10^5	1.53×10^5	1.91×10^5	1.53×10^5	1.91×10^5
Re_θ	5.20×10^3	5.31×10^3	1.33×10^3	2.04×10^3	6.34×10^3	6.19×10^3	8.85×10^2	8.87×10^2
δ (mm)	21.79	22.63	18.8	20.7	13.59	15.54	15.3	18.5
δ^*/δ	0.20	0.20	0.08	0.12	0.39	0.34	0.23	0.19
θ/δ	0.14	0.13	0.06	0.09	0.13	0.14	0.05	0.06

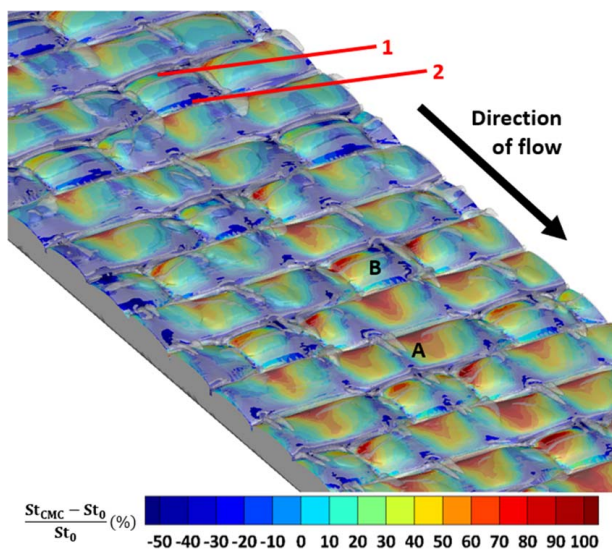


Fig. 12 Contour of St number augmentation for the 90-deg surface over which a q -criterion of 100,000 is displayed to indicate swirling structures

90-deg orientation (Fig. 10) indicates good agreement between the experimental and CFD results below $Y/\delta = 0.1$. However, above $Y/\delta = 0.1$, the displacement thickness is underdeveloped by 50% like the 0-deg surface. The near-wall behavior of the boundary layers for both weave orientations is predicted by the CFD; however, further from the wall, the CFD fails to properly predict the boundary layer thickness.

With the reasonable agreement between the CFD and experiments for the 0-deg case, the CFD is interrogated further, enabling a deeper understanding of the underlying physics. Figure 11 shows the velocity in the near-wall region as it passes over the most substantial St augmentation zones on the 0-deg surface. The positive St augmentation zone on the leading edge of the “B” tow shows the flow is impinging on the forward-facing surface. In front of this positive augmentation region, a negative St augmentation region is present. Here, a zone of reduced velocity is present before leading up to the impinging edge of a “B” tow, which is caused by the downward sloping surface and the recirculation caused by flow impinging on the “B” tow. On the downstream side of a “B” tow, a reduced velocity zone due to the slight downward slope of the tow can be seen resulting in the negative St augmentation seen in this region. Finally, in the region that has the largest positive St augmentation located on the front of an “A” tow just after a “B” tow, three separate flow features are responsible. First, directly behind the “B” tow, a recirculation is present, leading to reduced heat transfer in this small region. Downstream of the recirculation zone is a region of impingement as the flow passes over the recirculation zone from the downstream edge of a “B” tow, resulting in locally increased heat transfer. This impinging flow then continues downstream and accelerates over the upward facing upstream side of an “A” tow and is responsible for the last part of the locally increased heat transfer.

Figure 12 focuses on understanding the misprediction in the CFD for the 90-deg orientation, which exhibits more streaky behavior in the surface heat transfer in Fig. 8. The strong swirling flow structures over the 90 deg CMC surface are highlighted using the q -criterion. The q -criterion

$$q = \frac{1}{2} \left(-\frac{\partial u}{\partial y} \frac{\partial v}{\partial x} - \frac{\partial u}{\partial z} \frac{\partial w}{\partial x} - \frac{\partial v}{\partial z} \frac{\partial w}{\partial y} \right) - \frac{1}{2} \left(\left(\frac{\partial u}{\partial x} \right)^2 + \left(\frac{\partial v}{\partial y} \right)^2 + \left(\frac{\partial w}{\partial z} \right)^2 + \frac{\partial u}{\partial y} \frac{\partial v}{\partial x} + \frac{\partial u}{\partial z} \frac{\partial w}{\partial x} + \frac{\partial v}{\partial z} \frac{\partial w}{\partial y} \right) \quad (2)$$

is the second invariant of the velocity gradient tensor, with the first term in the parentheses representing the swirl and the second term representing the shear of the flow. By choosing a large positive value for the q -criterion, regions where strong swirling is present (i.e., coherent vortices) are shown. From these swirling regions, three distinct behaviors can be observed. The first occurs when an “A” tow transitions to a “B” tow, such as near location 1. The corners of the upstream side of the “B” tow produce three-pronged swirling structures. These structures correspond with regions of increased heat transfer in both the experimental and CFD results, suggesting the step down from an “A” tow to a “B” tow causes vortices to form along the edges of “B” tows.

The second group of flow structures present in Fig. 12 are the pairs of vortices that form on the leading edges of select “A” tows over negative augmentation streaks. These vortices form near the beginning of the test surface and develop into a repeating pattern of formation, dissipation, and then reformation with a period of five tows. The initial formation of these repeating stream-wise vortices stems from the crossing point of the “A” and “B” tows, but quickly deviates and becomes aligned off the center of the “B” tows. This alignment coincides with streaks of negative St augmentation in the CFD that are not present in the experimental results. It may be that these features are unsteady and have a smaller impact on the local heat transfer than predicted in steady RANS.

The third swirling features occur at the leading edges of each of the forward-facing tows directly in front of the high augmentation regions. These spanwise oriented vortices are the result of RANS overpredicting the effect of the blockage of the leading edges. This overprediction leads to more flow acceleration over the front of the tows, resulting in higher levels of predicted heat transfer than indicated by the experiments.

Effect of Weave Features on Adiabatic Effectiveness. The introduction of film cooling holes into the CMC surface offers insight into the impact that weave patterns have on adiabatic film cooling effectiveness and flowfield characteristics. Adiabatic effectiveness contours of 7–7–7 holes at a blowing ratio of 1.5 are shown in Fig. 13. The smooth surface baseline is included, as well as the

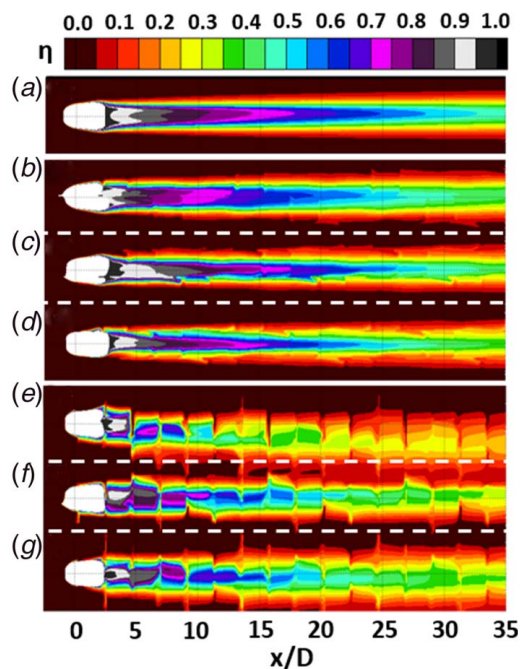


Fig. 13 Adiabatic effectiveness contours at $M=1.5$ for (a) flat plate, (b) 0-deg surface hole b, (c) 0-deg surface hole c, (d) 0-deg surface hole d, (e) 90-deg surface hole e, (f) 90-deg surface hole f, and (g) 90-deg surface hole g

three holes for each of the CMC surface orientations. The flat surface case shown in Fig. 13(a) shows similar characteristics but overpredicts the centerline and underpredicts the spreading compared to the experimental results shown by Schroeder and Thole [25]. Figure 13 indicates substantial variations between the holes for the CMC surfaces. Holes (b), (c), and (d) show variations between the three holes of the 0-deg surface, where they demonstrate performance close to or lower than the smooth surface baseline of hole (a). With significant lateral spreading and clear loss of centerline effectiveness, hole (b) also shows some slight asymmetry that starts at the hole exit. Holes (c) and (d) show some asymmetry but are overall symmetric about their centerlines with a slight increase in lateral spreading over the length of the domain.

Holes (e), (f), and (g) in Fig. 13 indicate how the 90-deg surface impacts the adiabatic effectiveness. Between the three holes shown for the 90-deg surface, the amount of local variation between the holes is greater than seen for the 0-deg case. Hole (e) shows more lateral spreading than hole (a) over the flat surface and has a large shift toward hole (f) before eventually joining hole (f) at $x/D = 20$. The centerline effectiveness for hole (d) degrades much faster than hole (a) over the flat surface; additionally, hole (d) has discrete regions of maximum effectiveness that correspond to the surface of individual tows. These gaps in maximum effectiveness are explored later. Hole (f) has a similar decrease in maximum adiabatic effectiveness values to hole (e) and an increase in lateral spreading compared to the flat baseline but less than hole (e). Hole (f) stays mostly centered, even keeping its maximum adiabatic effectiveness values centered after $x/D = 25$ where it merges with hole (e). The third 90-deg hole, hole (g), shows similar characteristics to hole (f), with more lateral spreading than hole (f) but less than hole (e).

At a higher blowing ratio of $M = 3$ (Fig. 14), many of the same characteristics from $M = 1.5$ are observed. On the 0-deg surface, holes (b), (c), and (d) show narrower effectiveness profiles due to jet detachment as would be expected at the higher blowing ratio, but they still have greater lateral coverage than the flat baseline hole (a). The three holes on the 90-deg surface show less of sensitivity-to-blowing ratio, with hole (e) showing an improvement in adiabatic effectiveness down the centerline with higher values

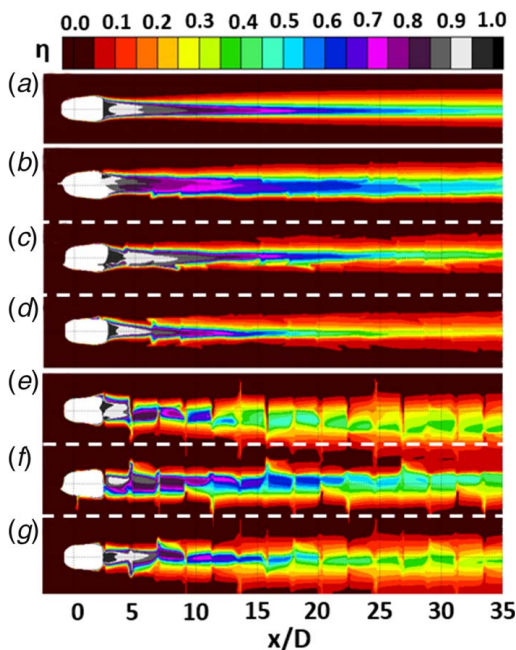


Fig. 14 Adiabatic effectiveness contours at $M = 3.0$ for (a) flat plate, (b) 0-deg surface hole b, (c) 0-deg surface hole c, (d) 0-deg surface hole d, (e) 90deg surface hole e, (f) 90deg surface hole f, and (g) 90deg surface hole g

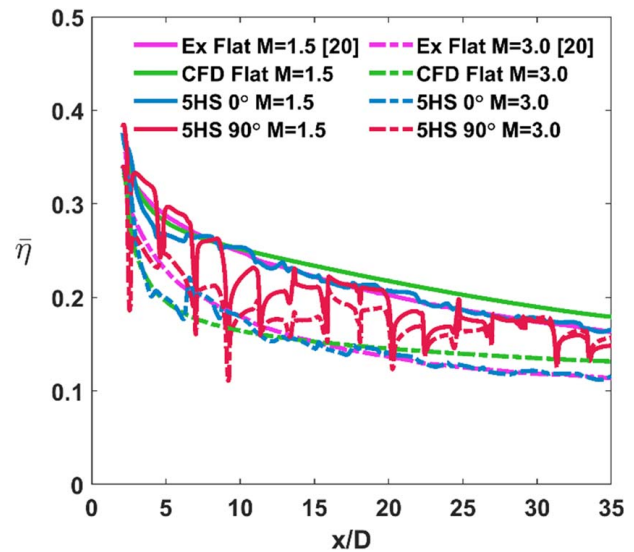


Fig. 15 Laterally averaged adiabatic effectiveness for the six CFD cases investigated and two experimental cases from Schroeder and Thole [20]

permeating further downstream for the $M = 3$ case compared to the $M = 1.5$ case. Additionally, hole (e) experiences a smaller shift toward hole (f) at the higher blowing ratio, but still drifts toward hole (f) before joining near $x/D = 25$. Holes (e), (f), and (g) all experience a reduction in lateral spreading at $M = 3$ compared to their $M = 1.5$ counterparts.

Figure 15 shows the laterally averaged adiabatic effectiveness taken across all three holes for the 0-deg and 90-deg surfaces and across the single hole of the flat surface across both blowing ratios. The smooth case is also compared to the experimental data taken by Schroeder and Thole [20]. At $M = 1.5$, the CFD results are in good agreement close to the hole, but slightly overpredict $\bar{\eta}$ further downstream, while for $M = 3$, the CFD underpredicts from $0 < x/D < 15$ and then slightly overpredicts at $x/D > 15$. In general, however, the flat surface CFD is in reasonable agreement with prior experimental data.

From Fig. 15, the visual similarities between the 0-deg surface and the flat baseline observed in Figs. 13 and 14 manifest as similar laterally averaged performance for a given blowing ratio. From $0 < x/D < 20$ the 0 deg and flat baseline cases are very similar at both $M = 1.5$ and $M = 3$. Downstream of $x/D = 20$, the 0-deg surface has lower adiabatic effectiveness values than the flat surface. This comparative performance loss is due to the 0-deg surface moving the counter-rotating vortex pair (CRVP) further from the wall, which will be further investigated later in this paper. The lateral averaged adiabatic effectiveness values for the 90-deg surface also shown in Fig. 15 have very different behavior. One of the most striking features of the 90-deg surface is the clear indication of where each streamwise tow transition is located, with substantial drops in effectiveness at these locations. Between the hole exit and $x/D = 5$ both the $M = 1.5$ and $M = 3$, blowing ratios have laterally averaged adiabatic effectiveness higher than the other two surfaces at the equivalent blowing ratio. This is likely because the tow transition directly at the hole exit causes increased mixing that spreads the coolant around the hole exit in a wider region than the holes in the other surfaces do. The difference between the two laterally averaged 90-deg blowing ratios starts around $\eta = 0.1$, but quickly decreases where the two blowing ratios have similar performance at $x/D = 20$. This convergence of laterally averaged effectiveness suggests an insensitivity in blowing ratio for the 90-deg surface. This insensitivity is likely due to the increased spreading caused by the between the CMC surface and flowfield drawing coolant back toward the wall.

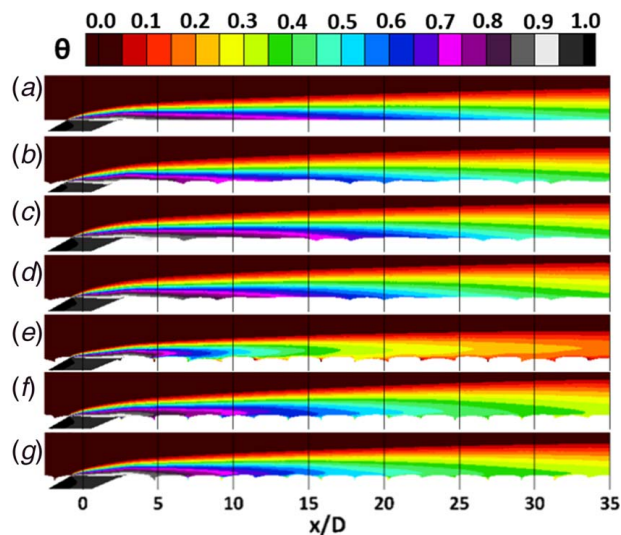


Fig. 16 Centerline temperature contours at $M = 1.5$ for (a) flat plate, (b) 0-deg surface hole b, (c) 0-deg surface hole c, (d) 0-deg surface hole d, (e) 90-deg surface hole e, (f) 90-deg surface hole f, and (g) 90-deg surface hole g

Impact of Weave Features on Coolant Flowfields. Figure 16 shows nondimensional temperature profiles of the seven different hole cases on the hole centerline, at a blowing ratio of 1.5. Holes (b) and (d) on the 0-deg surface show a reduction in coolant along the centerline compared to the flat surface hole (a). The temperature profile of hole (c) is similar to the profile of flat surface hole (a) with $\theta = 0.7$ values, reaching $x/D = 17$ for both holes. Additionally, holes (c) and (d) have thicker boundary layers than hole (a), suggesting increased mixing between the coolant and the mainstream. Temperature profiles for the holes in the 90-deg oriented surface, holes (e), (f), and (g) show the impact the weave has on the coolant in multiple ways. All three 90-deg holes show lower coolant levels from the hole exit to the end of the domain compared to hole (a). The 90-deg surface also enables the coldest flow to pass over the edges of the tows leaving regions of higher coolant temperatures between the tows. A good example from Fig. 16 is at the wall for hole (e) at $x/D = 16$ where the channel between two tows is at a higher temperature (lower nondimensional temperature) than the tops of the tow to either side. This behavior leads to bands of lower adiabatic effectiveness seen in Fig. 13 and the sudden drops in laterally averaged effectiveness in Fig. 15.

Cross-planes of all seven holes are shown in Fig. 17 at $x/D = 4$ showing streamlines plotted over nondimensional temperature contours at a blowing ratio of 1.5. Here, the streamlines show the size and core location of the CRVP that was observed by Schroeder and Thole [25] when the 7-7-7 hole interacts with the freestream but note that they do not indicate the strength of the vortices. Underneath the cross-planes are adiabatic effectiveness contours that end at the location of the cross-plane, which provide some context for the temperature fields and streamlines in the cross-planes. Hole (b) on the 0-deg surface shows the CRVP, but unlike the flat case of hole (a), one of the vortices has shifted toward the center and is lying in the channel created between two tows. The center hole, hole (c), on the 0-deg surface has no major change to the CRVP and has a different but similar temperature profile to the flat baseline. Hole (d) shares the most commonality with the baseline, with both the nondimensional temperature profile and CRVP location similar.

The 90-deg surface results in more deviation in the flowfield than the 0-deg surface, which is best highlighted by hole (e). Near $z/D = -9$, an unexpected vortex is present outside the coolant field; this may be due to unexpected influence by the symmetry boundary condition imposed along the sides of the domain. At $z/D = -7$, the expected vortex is present but its counterpart is missing. This unexpected vortex arrangement has little impact on the coolant this close to the hole with the temperature field still roughly symmetric about $z/D = -6$, the midplane of hole (e). Hole (f) is located at $z/D = 0$ and has a mismatched CRVP. The vortex near $z/D = -1$ is higher and larger than the one located at $z/D = 1$. This is likely because of the missing vortex for hole (e) allowing the vortex located at $z/D = -1$ to develop more strongly. This vortex in turn is pulling the coolant from hole (f) up and over toward hole (e) as shown in Fig. 17. The film cooling jet from the third hole for the 90-deg case (hole (g)) immediately encounters the tow directly after the hole and shows increased lateral spreading compared to the baseline but has no significant deviation in the CRVP structure.

Figure 18 shows cross-planes at $x/D = 10$ to understand the impact the weave pattern has on coolant as it progresses downstream. At $x/D = 10$, hole (b) has one vortex shift toward $z/D = -9$ and further away from the surface. The other vortex in the CRVP shifts toward $z/D = -3$ and closer to the wall, centering above the gap between two tows. This mismatched pair of vortices results in little impact on the overall temperature field; this is likely because the parts of the vortices that are closest to the coolant fields are similar in size despite the cores of the vortices being in different locations. Holes (c) and (d) do not show any major changes to the flowfield, with both CRVPs positioned similarly to the baseline

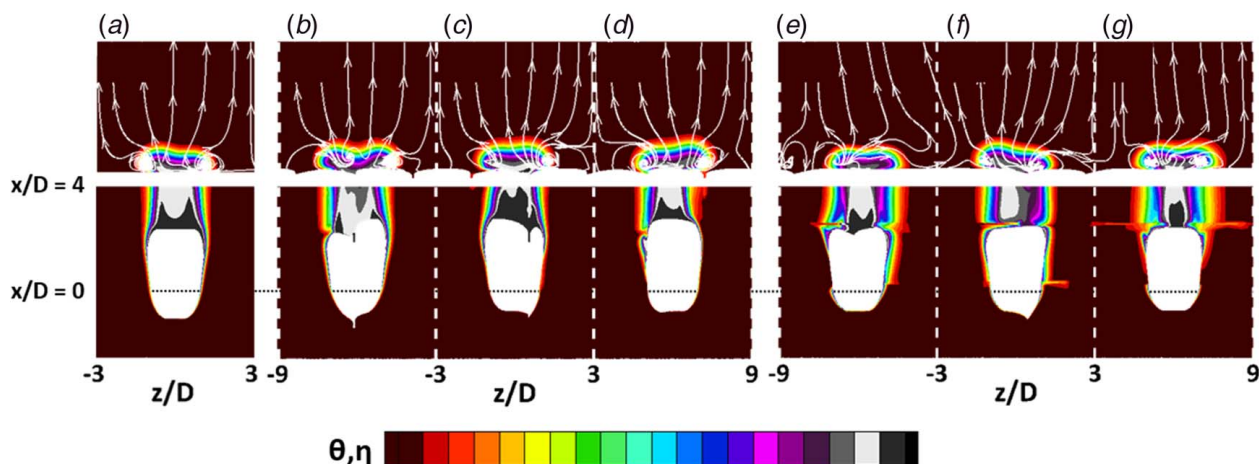


Fig. 17 Temperature cross-planes at $M = 1.5$ and $x/D = 4$ with η contours leading up to the cross-planes for (a) flat plate, (b) 0-deg surface hole b, (c) 0-deg surface hole c, (d) 0-deg surface hole d, (e) 90-deg surface hole e, (f) 90-deg surface hole f, and (g) 90-deg surface hole g

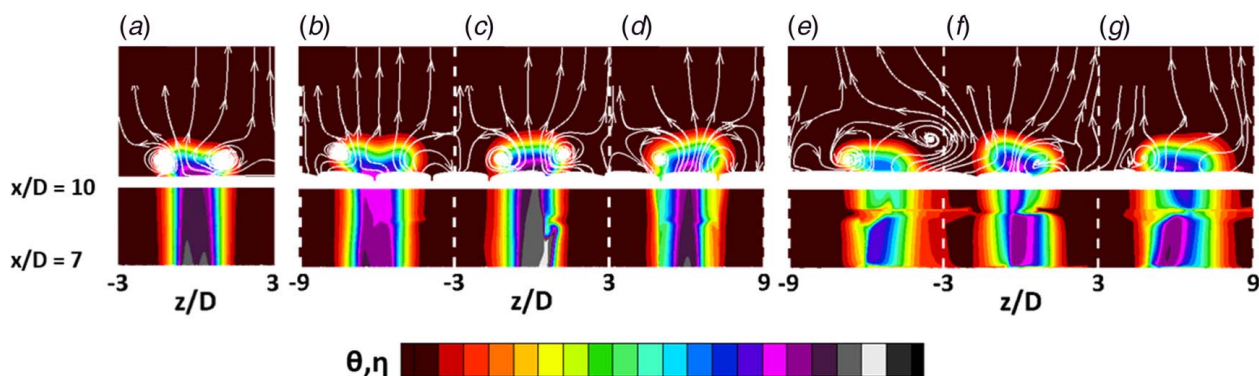


Fig. 18 Temperature cross-planes at $M=1.5$ and $x/D=10$ with η contours leading up to the cross-planes for (a) flat plate, (b) 0-deg surface hole b, (c) 0-deg surface hole c, (d) 0-deg surface hole d, (e) 90-deg surface hole e, (f) 90-deg surface hole f, and (g) 90-deg surface hole g

case. Across all three 0-deg surface holes, the temperature field indicated that the CMC surface promotes more mixing than the flat surface. This mixing results in lower centerline adiabatic effectiveness values but the increased lateral spread results in the 0-deg surface possessing similar lateral averaged values to the baseline shown in Fig. 15.

Downstream cross-planes of 90-deg surface shown in Fig. 18 indicate larger deviations in asymmetry and changes to the CRVP. Hole (e) still has the two vortices located near $z/D=-9$ and -7 similar to the cross-plane at $x/D=4$, but the vortex that initially is present near the coolant jet of hole (f) shifts toward hole (e) ending up at $z/D=-3.5$. This vortex located almost directly between the two holes is pulling the coolant from hole (e) over toward hole (f), resulting in the centerline of hole (e) shifting and the increased lateral spreading seen in Fig. 18. The shift of this vortex also results in the increase in the mixing of hole (f) on the side nearest to the shifted vortex. On the other side of hole (f), the vortex located at $z/D=1$ has very little movement at progress from $x/D=4$ to $x/D=10$. Hole (g) has its CRVP in roughly the same position as the flat baseline but experiences more mixing than the flat case of hole (a).

Conclusions

Two CMC weave orientations were investigated in a conjugate heat transfer study to investigate the ability of RANS to evaluate the convective heat transfer and near-wall flow field over the weave surface. Then the same two weave geometries were used to investigate the impact on film cooling.

The investigation into the ability of RANS to predict the heat transfer and flowfield over a CMC weave surface resulted in similar prediction accuracies seen from previous rough surfaces [10,11]. CFD prediction of the 0-deg surface is able to capture the local heat transfer trends and near-wall flow behavior, although accuracy in local values near reattachment/separation is not quite captured. The 90-deg surface sees significant differences between the experimental and computational heat transfer trends with several dominating structures present in the CFD that are not present in the experimental result. These trends lead to the overprediction of heat transfer.

Film cooling is investigated across multiple different exit shapes and CMC surfaces, with the 0-deg and 90-deg surfaces impacting 7–7 film cooling holes differently. The 0-deg surface sees little impact compared to a traditional flat surface, both across multiple holes with slightly different hole exits and multiple blowing ratios. The only major difference is a slight decrease in centerline effectiveness, slight increase in lateral spreading, and an increase in the asymmetry of the coolant pattern.

The 90-deg surface had a larger impact on film cooling performance. The exposed tows facing perpendicularly to the freestream

and coolant cause lateral dispersion of coolant, resulting in narrow regions of increased lateral cooling and also narrow bands of decreased lateral cooling. Interactions between the weave and the holes can result in shifting of the CRVP that leads to increased mixing between the coolant and the mainstream. Although the steady RANS here would not predict vortex wandering behavior, the true behavior is likely prone to wandering which would result in further lateral spreading. The increased mixing due to the weave results in loss of performance near the hole, but leads to less sensitivity of cooling effectiveness with blowing ratio.

RANS predictions for flow over the 5 Harness Satin weave pattern selected are able to capture some of the local heat transfer and flowfield performance, especially for the 0-deg case, but fall short on accurately predicting the entire domain. Film cooling simulations predict the CMC surface increases lateral spreading with the 90-deg surface predicted to have a larger negative impact on film cooling than the 0-deg surface. Of the two weave orientations, the 0-deg weave orientation is most advantageous for the designer as it results in lower heat transfer and more predictable film cooling.

Acknowledgment

The authors would like to thank Pratt and Whitney for their generous support over the duration of this project.

Conflict of Interest

There are no conflicts of interest.

Data Availability Statement

The data sets generated and supporting the findings of this article are obtainable from the corresponding author upon reasonable request. The data and information that support the findings of this article are freely available online.² The authors attest that all data for this study are included in the paper. Data provided by a third party listed in Acknowledgment.

Nomenclature

- k = thermal conductivity
- h = heat transfer coefficient, $h = q''/(T_s - T_\infty)$
- t = local thickness
- x = streamwise direction
- y = wall normal direction
- z = spanwise direction

²<https://sites.psu.edu/turbine/>

A = hole cross-sectional area
 D = diameter of film cooling holes
 L = film cooling hole length
 M = blowing ratio, $\rho_c U_c / \rho_\infty U_\infty$
 P = pitch between film cooling holes
 U = mean streamwise velocity
 C_p = specific heat at constant pressure
 S_a = arithmetic mean roughness
 S_q = root mean square roughness
 S_z = maximum roughness height
 T_{Al} = aluminum temperature
 T_s = plate surface temperature
 \dot{m}_c = coolant mass flowrate
 q_{cond} = heat flux from conduction
 q_{rad} = heat flux from radiation
 AR = area ratio, A_{exit}/A_{inlet}
 $5HS$ = five-Harness Satin (weave type)
 Pr = Prandtl number
 Re_x = Reynolds number, $Re_x = U_\infty x / \nu$
 Re_θ = momentum thickness Reynolds number, $Re_\theta = U_\infty \theta / \nu$
 St = Stanton number, $St = h / (\rho C_p U_\infty)$

Greek Symbols

α = hole injection angle
 β = expansion angle for diffused outlet
 δ = boundary layer thickness
 δ^* = displacement thickness
 η = local adiabatic effectiveness, $(T_\infty - T_{aw}) / (T_\infty - T_c)$
 θ = momentum thickness
 θ = fluid temperature, $(T_\infty - T) / (T_\infty - T_c)$
 λ = tow width
 λ_{30} = tow width for 30× scaled geometry
 ρ = density
 ν = kinematic viscosity

Subscripts

air = property of air
 CMC = property of CMC surface test plate
 $diff$ = diffuser section
 $exit$ = exit plane of the film cooling hole
 fwd = forward expansion of shaped hole
 $inlet$ = inlet plane of the film cooling hole
 lat = lateral expansion of shaped hole (half-angle)
 m = metering section
 0 = property of a flat surface
 ∞ = freestream

References

- [1] Walock, M. J., Heng, V., Nieto, A., Ghoshal, A., Murugan, M., and Driemeyer, D., 2018, "Ceramic Matrix Composite Materials for Engine Exhaust Systems on Next-Generation Vertical Lift Vehicles," *ASME J. Eng. Gas Turbines Power*, **140**(10), p. 102101.
- [2] Cinibulk, M. K., Apostolov, Z. D., Boakye, E. E., Key, T. S., and King, D. S., 2018, "Constituent Development for Higher-Temperature Capable Ceramic Matrix Composites," Proceedings of the ASME Turbo Expo, Oslo, Norway, June 11–15, ASME Paper No. GT2018-76835.
- [3] Wilkins, P. H., Lynch, S. P., Thole, K. A., Quach, S., and Vincent, T., 2021, "Experimental Heat Transfer and Boundary Layer Measurements on a Ceramic Matrix Composite Surface," *ASME J. Turbomach.*, **143**(6), p. 061010.
- [4] Goldstein, R. J., Eckert, E. R. G., Chiang, H. D., and Elovic, E., 1985, "Effect of Surface Roughness on Film Cooling Performance," *ASME J. Eng. Gas Turbines Power*, **107**(1), pp. 111–116.
- [5] Barlow, D. N., and Kim, Y. W., 1995, "Effect of Surface Roughness on Local Heat Transfer and Film Cooling Effectiveness," Proceedings of the ASME Turbo Expo, Houston, TX, June 5–8, ASME Paper No. 95-GT-14.
- [6] Schmidt, D. L., Sen, B., and Bogard, D. G., 1996, "Effects of Surface Roughness on Film Cooling," Proceedings of ASME Turbo Expo, Birmingham, UK, June 10–13, ASME Paper No. 96-GT-299.
- [7] Schmidt, D. L., and Bogard, D. G., 1996, "Effects of Free-Stream Turbulence Adn Surface Roughness on Film Cooling," Proceedings of the ASME Turbo Expo, Birmingham, UK, June 10–13, ASME Paper No. 96-GT-462.
- [8] Lawson, S. A., and Thole, K. A., 2011, "Effects of Simulated Particle Deposition on Film Cooling," *ASME J. Turbomach.*, **133**(2), p. 021009.
- [9] Bons, J. P., 2010, "A Review of Surface Roughness Effects in Gas Turbines," *ASME J. Turbomach.*, **132**(2), p. 021004.
- [10] Wang, Z. J., Chi, X. K., Shih, T., and Bons, J., 2004, "Direct Simulation of Surface Roughness Effects with RANS and DES Approaches on Viscous Adaptive Cartesian Grids," Proceedings of the 34th AIAA Fluid Dynamics Conference and Exhibit, Portland, OR, June 28–July 1, AIAA Paper No. 2004-2420.
- [11] Bons, J. P., McClain, S. T., Wang, Z. J., Chi, X., and Shih, T. I., 2008, "A Comparison of Approximate Versus Exact Geometrical Representations of Roughness for CFD Calculations of Cf and St," *ASME J. Turbomach.*, **130**(2), p. 021024.
- [12] Hanson, D. R., McClain, S. T., Snyder, J. C., Kunz, R. F., and Thole, K. A., 2019, "Flow in a Scaled Turbine Coolant Channel with Roughness Due to Additive Manufacturing," Proceedings of the ASME Turbo Expo, ASME Paper No. GT2019-90931.
- [13] Kapsis, M., and He, L., 2018, "Analysis of Aerothermal Characteristics of Surface Microstructures," *ASME J. Fluids Eng.*, **140**(5), p. 051104.
- [14] Kohli, A., and Thole, K. A., 1998, "Entrance Effects on Diffused Film-Cooling Holes," Proceedings of the ASME Turbo Expo, Stockholm, Sweden, June 2–5, ASME Paper No. 98-GT-402.
- [15] Haydt, S., Lynch, S., and Lewis, S., 2017, "The Effect of a Meter-Diffuser Offset on Shaped Film Cooling Hole Adiabatic Effectiveness," *ASME J. Turbomach.*, **139**(9), p. 091012.
- [16] Jones, F. B., Fox, D. W., and Bogard, D. G., 2019, "Evaluating the Usefulness of RANS in Film Cooling," Proceedings of the ASME Turbo Expo, Phoenix, AZ, June 17–21, ASME Paper No. GT2019-91788.
- [17] Harrison, K. L., and Bogard, D. G., 2007, "CFD Predictions of Film Cooling Adiabatic Effectiveness for Cylindrical Holes Embedded in Narrow and Wide Transverse Trenches," Proceedings of the ASME Turbo Expo, Montreal, Canada, May 14–17, ASME Paper No. GT2007-2800.
- [18] Haydt, S., and Lynch, S., 2019, "Cooling Effectiveness for a Shaped Film Cooling Hole at a Range of Compound Angles," *ASME J. Turbomach.*, **141**(4), p. 041005.
- [19] Nemeth, N. N., Mital, S. K., and Lang, J., 2010, "Evaluation of Solid Modeling Software for Finite Element Analysis of Woven Ceramic Matrix Composites," NASA Report No. NASA T/M 2010-216250.
- [20] Schroeder, R. P., and Thole, K. A., 2014, "Adiabatic Effectiveness Measurements for a Baseline Shaped Film Cooling Hole," Proceedings of the ASME Turbo Expo, Dusseldorf, Germany, June 16–20, ASME Paper No. GT2014-25992.
- [21] Eberly, M. K., and Thole, K. A., 2014, "Time-Resolved Film-Cooling Flows at High and Low Density Ratios," *ASME J. Turbomach.*, **136**(6), p. 061003.
- [22] Silieti, M., Kassab, A. J., and Divo, E., 2005, "Film Cooling Effectiveness: Comparison of Adiabatic and Conjugate Heat Transfer CFD Models," Proceedings of the ASME Turbo Expo, Reno-Tahoe, NV, June 6–9, ASME Paper No. GT2005-68431.
- [23] Hoda, A., and Acharya, S., 1999, "Predictions of a Film Coolant Jet in Crossflow With Different Turbulence Models," *ASME J. Turbomach.*, **122**(3), pp. 558–569.
- [24] Ferguson, J. D., Walters, D. K., and Leyle, J. H., 1998, "Performance of Turbulence Models and Near-Wall Treatments in Discrete Jet Film Cooling Simulations," Proceedings of the ASME Turbo Expo, Stockholm, Sweden, June 2–5, ASME Paper No. 98-GT-438.
- [25] Schroeder, R. P., and Thole, K. A., 2016, "Effect of High Freestream Turbulence on Flowfields of Shaped Film Cooling Holes," *ASME J. Turbomach.*, **138**(9), p. 091001.